Leading-order cross term correction of three-dimensional parabolic equation models

Frédéric Sturm[a)]

Laboratoire de Mécanique des Fluides et d'Acoustique, Unité Mixte de Recherche, Centre National de la Recherche Scientifique 5509, Université de Lyon, École Centrale de Lyon, 36 avenue Guy de Collongue, F-69134 Ecully Cedex, France

The issue of handling a leading-order cross-multiplied term in three-dimensional (3D) parabolic equation (PE) based models is addressed. In particular, numerical results obtained incorporating a leading-order cross-term correction in an existing 3D PE model, written in cylindrical coordinates, based on higher-order Padé approximations in both depth and azimuth, and a splitting operator technique are reported. Note that the numerical algorithm proposed in this paper could be used in the future to update any 3D PE codes that neglect cross terms and use a splitting numerical technique. The 3D penetrable wedge benchmark problem is chosen to illustrate the accuracy of the now-fully wide-angle enhanced 3D PE model. The comparisons with a 3D reference solution based on the image source clearly show that handling the leading-order cross term in the 3D PE computation is sufficient to remove the phase errors inherent to any 3D PE models that neglect cross terms in their formulations. © 2016 Acoustical Society of America.
[http://dx.doi.org/10.1121/1.4939735]

I. INTRODUCTION

Wide-angle parabolic equation (PE) based models are efficient and accurate tools for solving sound wave propagation problems in three-dimensional (3D) oceanic waveguides.[1–13] The reader is also referred to Refs. 8 and 14 for detailed reviews of 3D PE-based models. For practical reasons, most of them neglect cross-multiplied operator terms that appear naturally in wide-angle square root operator approximations of the 3D Helmholtz equation. It has been shown recently, both numerically and theoretically, that the use of a series of higher-order cross terms in a 3D PE model allows a notable reduction of the phase errors inherent to any PE computation, and can thus handle greater propagation angles.[10] Note that the cross terms were efficiently incorporated in a split-step Padé 3D PE algorithm that uses a Cartesian coordinate system (x, y, z), with x, y the two horizontal coordinates, and z the depth. In particular, it was shown that 3D PE computations carried out ignoring cross terms led to incorrect curvature of the horizontal (xy-plane) interference pattern in the transmission loss field. Among the 3D PE codes that are used by the underwater acoustic community, several consider a cylindrical coordinate system (r, θ, z) with r the horizontal range, θ the azimuthal angle, and z the depth below the ocean surface. Although the 3D PE solutions obtained without cross term corrections and written in cylindrical coordinates, intrinsically contain a better curvature of the horizontal interferences, simply due to the nature of the coordinate system used, some phase errors are still present (as shown in Ref. 8).

The objective of the present paper is to confirm the necessity of cross terms in 3D PE-based formulations and to show that a leading-order cross term correction can be

sufficient to remove phase errors in 3D solutions obtained by 3D PE computations in cylindrical coordinates. The leading-order cross term is incorporated in an existing 3D PE model[8] based on high-order Padé approximations in both depth and azimuth, and a splitting operator technique. The paper is organized as follows. The newly wide-angle 3D PE model that includes the leading-order cross term is derived in Sec. II and then discretized in Sec. III. In particular, various aspects of the numerical technique used to handle the additional leading-order cross term are detailed. The improved accuracy of the now-fully wide-angle 3D PE model is then assessed on the classical 3D Acoustical Society of America (ASA) wedge benchmark problem.[3,8,10] Finally, advantages and drawbacks of the proposed numerical model are summarized and forthcoming improvements are discussed in Sec. V. Preliminary results of the present work were presented during the "2nd International Conference and Exhibition on Underwater Acoustics" held in Rhodes, Greece, in 2014.

II. MODEL DESCRIPTION

We consider a multilayered waveguide composed of one water layer and one or several fluid sediment layers. The geometry of each layer is fully 3D. Cylindrical coordinates are used where r, θ, and z represent, respectively, the horizontal range, the azimuthal angle, and the depth (increasing downwards) below the ocean surface. Considering a harmonic point source of frequency f, located at $r = 0$ and $z = z_S > 0$, and assuming only outward propagation in range, the elliptic-type 3D Helmholtz equation can be replaced by the following one-way equation:

$$\partial_r \psi = ik_0(\sqrt{\mathcal{Q}} - \mathcal{I})\psi, \tag{1}$$

a)Electronic mail: frederic.sturm@ec-lyon.fr

where $\psi = \psi(r, \theta, z)$ is the acoustic field related to the acoustic pressure by

$$P(r, \theta, z) = H_0^{(1)}(k_0 r) \times \psi(r, \theta, z),$$

with $H_0^{(1)}$ the zeroth-order Hankel function of the first kind, and $k_0 = 2\pi f / c_{\text{ref}}$ with c_{ref} a reference sound speed. In Eq. (1), $\mathcal{I}$ denotes the identity operator and $\mathcal{Q} = \mathcal{I} + \mathcal{X} + \mathcal{Y}$ with $\mathcal{X}$ the two-dimensional (2D) depth operator in the rz-plane and $\mathcal{Y}$ the azimuthal operator, defined as

$$\mathcal{X} = (n_\alpha^2 - 1)\mathcal{I} + \frac{\rho}{k_0^2} \partial_z(\rho^{-1}\partial_z), \quad \mathcal{Y} = \frac{1}{(k_0 r)^2} \partial_\theta^2.$$

Here, $n_\alpha(r, \theta, z) = (c_{\text{ref}}/c(r, \theta, z))\,(1 + i\eta\alpha)$ denotes the complex (to account for lossy layers) index of refraction, with c the sound speed, α the attenuation coefficient expressed in decibels per wavelength, and $\eta = 1/(40\pi \log_{10} e)$, and ρ denotes the density, constant within each layer.

3D PEs are obtained considering various approximations of the square root operator $\sqrt{\mathcal{Q}}$ (see Sec. 6.8 of Ref. 14). For instance, the original 3D PE derived by Tappert[15] can be derived by expanding $\sqrt{\mathcal{Q}}$ in a Taylor series and retaining only the linear terms in $\mathcal{X}$ and $\mathcal{Y}$,

$$\sqrt{\mathcal{Q}} \approx \mathcal{I} + \frac{1}{2}(\mathcal{X} + \mathcal{Y}). \tag{2}$$

The resulting PE (known as the standard 3D PE) has a narrow-angle capability in both depth and azimuth. Though 3D PE formulations based on other approximations exist (see, for instance, Refs. 16–19), most of the higher-order 3D PE codes are based on the following approximation:

$$\sqrt{\mathcal{Q}} \approx -\mathcal{I} + \sqrt{\mathcal{I} + \mathcal{X}} + \sqrt{\mathcal{I} + \mathcal{Y}}. \tag{3}$$

Any higher-order approximation based on Taylor or Padé series expansions of the two square root operators $\sqrt{\mathcal{I} + \mathcal{X}}$ and $\sqrt{\mathcal{I} + \mathcal{Y}}$ can now be used. Clearly, such higher-order approximations, when incorporated in Eq. (3), lead to 3D PEs that advantageously separate the depth operator $\mathcal{X}$ from the azimuth operator $\mathcal{Y}$, thus allowing for the use of very-efficient (in a practical point of view) numerical algorithms similar to the alternating direction implicit (ADI) method. Depending on the quality of the approximation made in depth or in azimuth, one can obtain 3D PE models that have narrow-angle capabilities in both depth and azimuth,[15,20] a wide-angle capability in depth and a narrow-angle capability in azimuth,[1–3,5,9] or wide-angle capabilities in both depth and azimuth.[6–8] However, as noticed in Ref. 8, all 3D PE models that are based on the approximation given by Eq. (3) do not, strictly speaking, have a wide-angle capability since they neglect cross-derivative terms of the form of (or equivalent to) $\mathcal{X}\mathcal{Y}$, $\mathcal{X}\mathcal{Y}^2$, $\mathcal{X}^2\mathcal{Y}$, etc., that are present naturally in direct higher-order Taylor or Padé series expansions of the square root operator $\sqrt{\mathcal{I} + \mathcal{X} + \mathcal{Y}}$. As shown in Ref. 10, the use of such higher-order cross terms allows a non-negligible reduction of the phase errors inherent to any PE computation and can thus handle greater propagation angles.

Let us derive now fully wide-angle 3D PEs. Following Lin and Duda,[12] we first write the second-order Taylor series around $\sqrt{\mathcal{I} + \mathcal{X}} = \mathcal{I}$ and $\sqrt{\mathcal{I} + \mathcal{Y}} = \mathcal{I}$,

$$\begin{aligned}
\sqrt{\mathcal{Q}} \approx &-\mathcal{I} + \sqrt{\mathcal{I} + \mathcal{X}} + \sqrt{\mathcal{I} + \mathcal{Y}} \\
&- \frac{1}{2}\left(-\mathcal{I} + \sqrt{\mathcal{I} + \mathcal{X}}\right)\left(-\mathcal{I} + \sqrt{\mathcal{I} + \mathcal{Y}}\right) \\
&- \frac{1}{2}\left(-\mathcal{I} + \sqrt{\mathcal{I} + \mathcal{Y}}\right)\left(-\mathcal{I} + \sqrt{\mathcal{I} + \mathcal{X}}\right),
\end{aligned} \tag{4}$$

where the non-commutativity of operators $\mathcal{X}$ and $\mathcal{Y}$ has been kept. The square-root operators $\sqrt{\mathcal{I} + \mathcal{X}}$ and $\sqrt{\mathcal{I} + \mathcal{Y}}$ that appear in the two last product terms can then be approximated using various Taylor and Padé series expansions. By considering linear approximations,[21–23] $\sqrt{\mathcal{I} + \mathcal{X}} \approx \mathcal{I} + \frac{1}{2}\mathcal{X}$ and $\sqrt{\mathcal{I} + \mathcal{Y}} \approx \mathcal{I} + \frac{1}{2}\mathcal{Y}$, it leads to

$$\sqrt{\mathcal{Q}} \approx -\mathcal{I} + \sqrt{\mathcal{I} + \mathcal{X}} + \sqrt{\mathcal{I} + \mathcal{Y}} - \frac{1}{8}(\mathcal{X}\mathcal{Y} + \mathcal{Y}\mathcal{X}), \tag{5}$$

which is similar to the higher-order approximations used by Yevick and Thomson (see Refs. 21 and 22) and can be viewed as a leading-order correction of the basic approximation of Eq. (3). Neglecting azimuthal variations of the index of refraction, i.e., assuming that operators $\mathcal{X}$ and $\mathcal{Y}$ commute, leads to the following approximation:

$$\sqrt{\mathcal{Q}} \approx -\mathcal{I} + \sqrt{\mathcal{I} + \mathcal{X}} + \sqrt{\mathcal{I} + \mathcal{Y}} - \frac{1}{4}\mathcal{X}\mathcal{Y}. \tag{6}$$

Finally, the two square-root operators that remain in Eq. (6) can be approached using various wide-angle approximations. For instance, by using Padé approximations in both depth and azimuth, one obtains

$$\sqrt{\mathcal{Q}} \approx \mathcal{I} + \sum_{k=1}^{n_p} \frac{a_{k,n_p}\mathcal{X}}{\mathcal{I} + b_{k,n_p}\mathcal{X}} + \sum_{k=1}^{m_p} \frac{a_{k,m_p}\mathcal{Y}}{\mathcal{I} + b_{k,m_p}\mathcal{Y}} - \frac{1}{4}\mathcal{X}\mathcal{Y}, \tag{7}$$

where n_p and m_p are the number of Padé terms, respectively, in depth and azimuth, and where $a_{k,np}$, $b_{k,np}$, $1 \le k \le n_p$, and a_{k,m_p}, b_{k,m_p}, $1 \le k \le m_p$, are real or complex (to attenuate Gibb's oscillations) Padé coefficients.[24,25] In a practical point of view, the two Padé series expansions appearing in the right-hand side of Eq. (7) are very convenient since they allow for a very-wide angle propagation, respectively, in depth and azimuth, the corresponding angular limitations depending on the two parameters n_p and m_p selected by the user. Inserting now the paraxial approximation given in Eq. (7) in the one-way 3D Eq. (1), we obtain the following wide-angle 3D PE model:

$$\partial_r\psi = ik_0 \left[\sum_{k=1}^{n_p} \frac{a_{k,n_p}\mathcal{X}}{\mathcal{I} + b_{k,n_p}\mathcal{X}} + \sum_{k=1}^{m_p} \frac{a_{k,m_p}\mathcal{Y}}{\mathcal{I} + b_{k,m_p}\mathcal{Y}} - \frac{1}{4}\mathcal{X}\mathcal{Y} \right]\psi. \tag{8}$$

The now fully wide-angle capability of this 3D PE model is attributed to the presence of the last (cross-multiplied) term

Frédéric Sturm

in Eq. (8). The 3D PE model of Ref. 8, which uses separate Padé approximations in depth and in azimuth as in Eq. (8), has been modified to handle the leading-order cross-multiplied term. This is explained in Sec. III.

III. NUMERICAL SCHEME

The wide-angle 3D PE equation given in Eq. (8) is solved numerically using the following splitting method: Given the 3D field ψ at the discrete range r_n, ψ is obtained at the next discrete range r_{n+1} in three steps.

The first step consists in computing n_p intermediate fields denoted $u^{(1)}(\theta, z)$, $u^{(2)}(\theta, z)$,..., $u^{(n_p)}(\theta, z)$, by solving

$$[\mathcal{I} + \mu_-^{(k)} \mathcal{X}^{(n+1/2)}] u^{(k)}(\theta, z)$$
$$= [\mathcal{I} + \mu_+^{(k)} \mathcal{X}^{(n+1/2)}] u^{(k-1)}(\theta, z), \quad 1 \leq k \leq n_p,$$

for $0 \leq \theta \leq 2\pi$ and $0 \leq z \leq z_{\max}$, where $u^{(0)}(\theta, z) = \psi(r_n, \theta, z)$ and

$$\mu_\pm^{(k)} = b_{k,n_p} \pm \frac{ik_0 \Delta r}{2} a_{k,n_p}, \quad 1 \leq k \leq n_p,$$

with Δr denoting the increment in range. The discretization in depth is achieved using a piecewise-linear finite-element method. Denoting N and M, respectively, the number of mesh points in depth and azimuth, this first step requires the inversion for $1 \leq k \leq n_p$ of M algebraic linear systems of order N (with tridiagonal matrices), which corresponds to the calculation of the intermediate fields at successively adjacent azimuths $\theta_1, \theta_2,..., \theta_M$. Each set of linear equations is solved using a fast and robust direct (Gaussian) algorithm optimized for tridiagonal matrices.

The second step consists in computing m_p intermediate fields denoted $v^{(1)}(\theta, z)$, $v^{(2)}(\theta, z)$,..., $v^{(m_p)}(\theta, z)$, by solving

$$[\mathcal{I} + \nu_-^{(k)} \mathcal{Y}^{(n+1/2)}] v^{(k)}(\theta, z)$$
$$= [\mathcal{I} + \nu_+^{(k)} \mathcal{Y}^{(n+1/2)}] v^{(k-1)}(\theta, z), \quad 1 \leq k \leq m_p,$$

for $0 \leq \theta \leq 2\pi$ and $0 \leq z \leq z_{\max}$, where $v^{(0)}(\theta, z) = u^{(n_p)}(\theta, z)$, and

$$\nu_\pm^{(k)} = b_{k,m_p} \pm \frac{ik_0 \Delta r}{2} a_{k,m_p}, \quad 1 \leq k \leq m_p.$$

The discretization in azimuth is achieved using a higher-order centered finite difference (FD) scheme which allows a significant reduction of the required number of points in azimuth while still obtaining accurate solutions.[26] At each range step, handling the azimuthal coupling terms requires the inversion for $1 \leq k \leq m_p$ of N algebraic linear systems of order M, with entries in the upper right and lower left corners of the banded matrices to account for the continuity condition in azimuth. These inversions correspond to the calculation of the intermediate fields at fixed depths $z_1, z_2,..., z_N$. The bandwidth of the matrices depends on the order of the numerical azimuthal scheme. As in step 1, a direct (Gaussian) algorithm optimised for banded matrices is used.

The third step consists in computing $w^{(1)}(\theta, z)$, by solving

$$\left[\mathcal{I} + \frac{ik_0 \Delta r}{2} \times \frac{1}{4} (\mathcal{X}\mathcal{Y})^{(n+1/2)}\right] w^{(1)}(\theta, z)$$
$$= \left[\mathcal{I} - \frac{ik_0 \Delta r}{2} \times \frac{1}{4} (\mathcal{X}\mathcal{Y})^{(n+1/2)}\right] w^{(0)}(\theta, z),$$

for $0 \leq \theta \leq 2\pi$ and $0 \leq z \leq z_{\max}$, where $w^{(0)}(\theta, z) = v^{(m_p)}(\theta, z)$ and $\psi(r_{n+1}, \theta, z) = w^{(1)}(\theta, z)$. The discretization in both depth and azimuth is done using a second-order FD scheme, which leads to solving a system of linear equations which can be written in a compact matrix form as follows:

$$A\mathbf{x} = \mathbf{b}, \tag{9}$$

with A a nonsingular large square matrix of order $K = M \times N$ with complex elements, and with $\mathbf{x}$ and $\mathbf{b}$ complex-valued vectors of length K. Matrix A is a sparse 9-diagonal matrix with a block-tridiagonal structure. All the blocks are tridiagonal matrices of order M, with entries in the upper right and lower left corners due to the periodicity condition in azimuth. Note that the bandwidth of A being a function of M, the use of any direct algorithm as in steps 1 and 2, would require an excessive amount of memory storage (since storage must be allocated for the bandwidth in each row of matrix A) and limit significantly the number of mesh points. Therefore, in order to effectively utilize the sparseness of matrix A, an iterative (indirect) algorithm is used. Note that A being neither Hermitian, nor definite positive, it is difficult to invert A with standard iterative methods (like, for instance, the conjugate gradient method). Consequently, the original linear system given in Eq. (9) is replaced by the following linear system:

$$(Q^{-1}A)(Q^{-1}A)^* \mathbf{y} = Q^{-1}\mathbf{b}, \tag{10}$$

where Q denotes a square matrix of order K, introduced here to improve the conditioning of the original linear system (9) and where $(Q^{-1}A)^*$ denotes the complex conjugation and transposition of matrix $Q^{-1}A$. Note that Eq. (10) has been obtained by first multiplying Eq. (9) by a preconditioning matrix Q^{-1} and then by letting $\mathbf{x} = (Q^{-1}A)^* \mathbf{y}$. The conjugate gradient method can now be applied to solve Eq. (10) and the convergence of the preconditioned iterative algorithm (detailed in Ref. 18) is guaranteed due to the positive definite Hermitian property of matrix $(Q^{-1}A)(Q^{-1}A)^*$. Note that each loop of the iterative algorithm requires solving two auxiliary linear systems involving the preconditioning matrix Q and its adjoint Q*. Hence, the efficiency of this iterative algorithm highly depends on the preconditioning procedure. The preconditioning matrix Q must be chosen with care. For instance, adapting the preconditioning approach used by Bayliss et al. (see Ref. 27), the preconditioning matrix Q can be constructed using the tridiagonal matrices derived from the discretization of the depth operator $\mathcal{X}$ or the azimuthal operator $\mathcal{Y}$. In both cases, Q has a block-diagonal structure and, since each block of Q is a square tridiagonal matrix,

each inversion of Q can be performed using a direct algorithm optimized for tridiagonal matrices, as in steps 1 and 2. The numerical simulations shown in Sec. IV were performed with a preconditioner Q based on the discretization of the azimuthal operator $\mathcal{Y}$.

For 2D and $N \times 2D$ computations, both steps 2 and 3 are ignored and $\psi(r_{n+1}, \theta, z) = u^{(n_p)}(\theta, z)$. If step 3 is ignored, then $\psi(r_{n+1}, \theta, z) = v^{(m_p)}(\theta, z)$. It is important to notice that the convergence of the iterative algorithm used in step 3 deteriorates unreasonably when solving near $r = 0$. In order to bypass this problem, the computations are performed using a range-dependent number of points in azimuth:[18] at each step in range, the number of azimuthal points is selected such that the corresponding arc length increment $\Delta s = r \Delta \theta$ remains less than a given fraction (to be defined by the user) of the acoustic wavelength λ. In order not to deteriorate the quality of the discretization, the interpolation in azimuth is achieved at only specific discrete ranges.

IV. NUMERICAL RESULTS

To assess the accuracy of the newly developed wide-angle 3D PE model, we consider the now very-classical 3D ASA wedge benchmark (3D extension of the original 2D ASA wedge benchmark). An isotropic harmonic point source, emitting at 25 Hz, is placed at a depth of 100 m in a two-layer oceanic environment which consists of a lossless homogeneous water layer (sound speed: 1500 m/s, density: 1 g/cm^3) overlying a lossy half-space sediment bottom (sound speed: 1700 m/s, density: 1.5 g/cm^3, and absorption: 0.5 dB per wavelength), which leads to a critical grazing angle φ_c of approximately 28°. No shear energy is assumed in the bottom. The wedge-like tilted water/sediment interface is described by the surface $\{z = h(r, \theta)\}$ where

$$h(r, \theta) = 200 \left(1 - \frac{r \cos \theta}{4000} \right).$$

The water/sediment interface makes an angle of 2.86° with respect to the ocean surface at both $\theta = 0°$ (upslope direction) and $\theta = 180°$ (downslope direction) and is invariant along the $\theta = 90°$ and $\theta = 270°$ azimuthal directions. Note that the water depth at the source is 200 m. The 3D effects have been explained in detail by several authors and correspond to intramodal interference effects, leading to the succession of three zones across-slope, with three propagating modes present in zone I, two propagating modes in zone II, and only one propagating mode interfering with itself in zone III. Both 2D and 3D PE computations considered hereafter were carried out using $\Delta r = 10$ m and $\Delta z = 1$ m. The maximum computation range is 25 km and, unless specified otherwise, the reference sound speed c_{ref} is 1500 m/s and both 2D and 3D PE marching algorithms were initialized at $r = 0$ by a Greene's source.[28]

The 2D PE solution obtained with a Padé-2 approximation in depth (i.e., obtained with $n_p = 2$) is plotted in Fig. 1 and compared with a 2D reference solution (plotted as a gray curve) based on a normal mode expansion of the acoustic field. Recall that a 2D PE solution is computed ignoring both
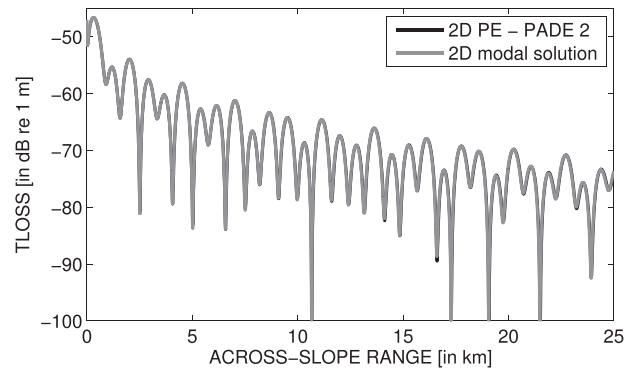

FIG. 1. Transmission loss (in dB re 1 m) curves at a receiver depth of 30 m in the across-slope direction $\theta = 90°$. The black curve corresponds to the 2D PE solution obtained using a Padé 2 ($n_p = 2$) approximation. The gray curve corresponds to a 2D reference (normal mode) solution.

steps 2 and 3 in the PE marching algorithm (see the discussion in Sec. III). The 2D solution is characterized by the interference effects of the three (initially present) propagating modes for all ranges. We observe that the 2D Padé-2 PE solution is in perfect agreement with the 2D normal mode solution, showing that no higher-order Padé approximation is required here for a 2D PE computation. Note that 2D PE solutions corresponding to lower-order parabolic approximations were also computed (solutions not shown here). Due to its angular limitation which is well below the critical grazing angle, the narrow-angle 2D PE solution poorly matched the 2D reference solution. The Padé-1 2D PE solution ($n_p = 1$) was in a much better agreement with the reference solution, though some discrepancies could still be observed at long ranges.

Let us turn now to the comparisons of fully-3D PE solutions with a 3D reference solution. Let us consider first 3D PE solutions obtained considering only steps 1 and 2 (i.e., ignoring step 3) in the marching algorithm in range. Several 3D PE solutions corresponding to different parabolic approximations in both depth and azimuth are plotted in Fig. 2. For each 3D PE computation, an eighth-order finite-difference azimuthal scheme with $M = 3240$ was used in step 2. The 3D reference solution, plotted as gray curves on each subplot, is based on the image source method (see, for instance, Ref. 29) and was originally provided by Westwood.[30] It shows that the transition distance between zones I and II, corresponding to the cut-off range of mode 3, is approximately equal to 11 km and the transition distance between zones II and III, corresponding to the cut-off range of mode 2, is around 16 km. Again, as expected, due to its angular limitation in both depth and azimuth, the narrow-angle 3D PE solution, plotted in Fig. 2(a), differs significantly in both phase and amplitude from the 3D reference solution for all ranges. Though the narrow-angle 3D PE solution exhibits qualitatively the same 3D effects predicted by the 3D reference solution, we observe that the outsets of zones II and III are shifted out in range by a few kilometers. The use of two wider-angle parabolic approximations in both depth and azimuth, see Fig. 2(b) ($n_p = 1 = m_p$) and Fig. 2(c) ($n_p = 2 = m_p$), allows a better agreement with the 3D reference solution, though a non-negligible shift in phase and in amplitude is
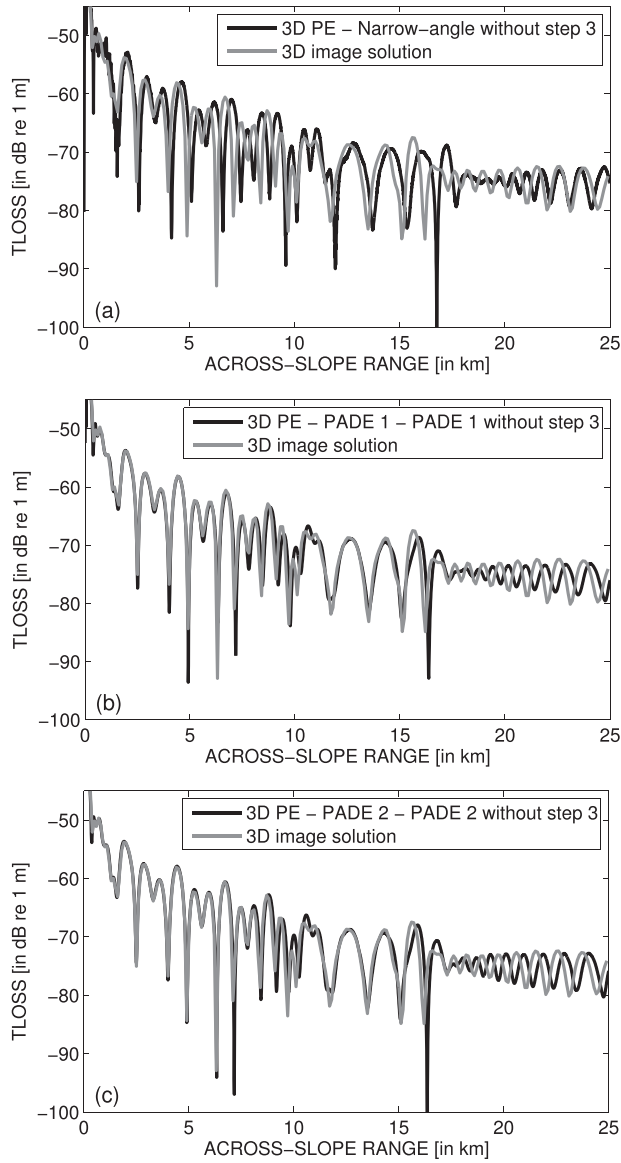
FIG. 2. Transmission loss (in dB re 1 m) curves at a receiver depth of 30 m in the across-slope direction $\theta = 90°$. The black curves correspond to 3D PE solutions obtained using (a) narrow-angle, (b) Padé 1 - Padé 1 ($n_p = 1 = m_p$), and (c) Padé 2 - Padé 2 ($n_p = 2 = m_p$) approximations, and computing without step 3. The gray curves correspond to a 3D reference (image) solution.

FIG. 3. Transmission loss (in dB re 1 m) curves at a receiver depth of 30 m in the across-slope direction $\theta = 90°$. The black curves correspond to 3D PE solutions obtained using (a) Padé 1 -Padé 1 ($n_p = 1 = m_p$) and (b) Padé 2 - Padé 2 ($n_p = 2 = m_p$) approximations, and computing with step 3. The gray curves correspond to a 3D reference (image) solution.

still present at some ranges, mainly in zone III where mode 1 interferes with itself, but also around the cut-off ranges of mode 3 (at ≈ 11 km) and mode 2 (at ≈ 16 km). The use of any higher-order approximation in depth and/or azimuth did not permit to reduce those shifts in phase and in amplitude (results not shown here).

Let us analyze now the effect on the 3D PE solutions of computations that handle the leading-order cross-derivative term. Two distinct wide-angle 3D PE solutions obtained incorporating step 3 in the marching algorithm are displayed in Fig. 3 and compared with the same 3D reference solution based on image sources. The wide-angle 3D PE solution corresponding to $n_p = 1 = m_p$ is displayed in Fig. 3(a). The wider-angle 3D PE solution shown in Fig. 3(b) was obtained considering $n_p = 2 = m_p$. Both 3D PE solutions were computed using $\Delta s \leq \lambda/6$ in step 3. We observe that both wide-angle 3D PE solutions displayed in Fig. 3 agree
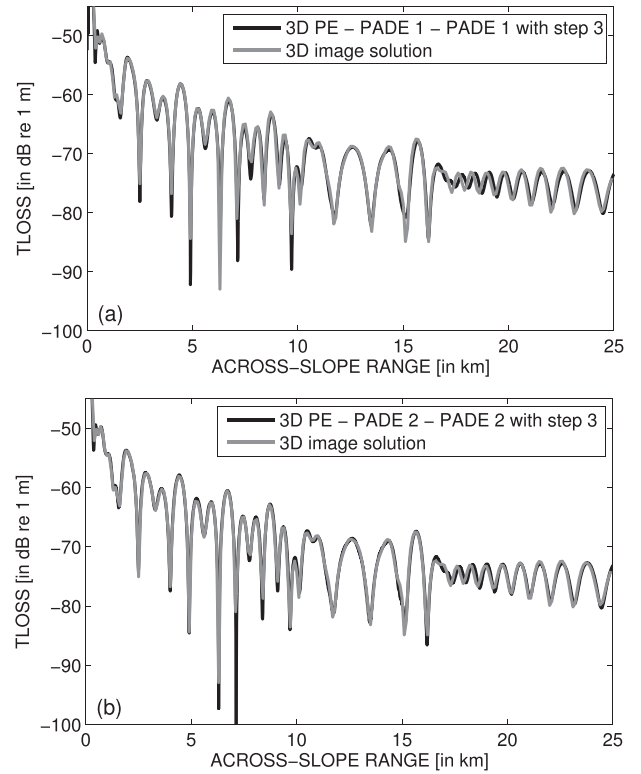
very well with the 3D reference solution. Upon closer inspection, we can observe that the 3D PE solution obtained with $n_p = 2 = m_p$ is, however, in slightly better agreement with the 3D reference solution. In particular, the large shift in phase present in all the 3D PE solutions obtained ignoring step 3 in the vicinity of the cut-off ranges of modes 2 (around 16 km) and mode 3 (around 11 km) or in the third zone where mode 1 interferes with its own echo, has been now reduced significantly. Comparisons of the 3D PE solutions obtained with and without step 3 and corresponding to different individual modal initializations are displayed in Fig. 4 and are coherent with the previous analysis.

To conclude, we displayed in Fig. 5 gray-scale images of the transmission loss (vertical slices in the across-slope direction) corresponding to the wide-angle 2D PE solution ($n_p = 2$) and the wide-angle 3D PE solutions ($n_p = 2 = m_p$) obtained with and without step 3. This allows us to better visualize in the 3D solutions the succession of the three zones across-slope. In particular, the vertical interference fringes characterizing the third zone (i.e., for ranges greater than ≈ 16 km) correspond to mode 1 interfering with itself. On the contrary, as explain before, the 2D solution exhibits for all ranges the interference pattern of the three propagating modes. Horizontal slices at a fixed depth of 30 m are displayed in Fig. 6. The differences between the 2D and 3D solutions are very weak in the vicinity of the source, but become more and more pronounced as the propagation range increases. Focusing now on the 3D PE solutions, we observe an overall similarity between the two 3D PE fields displayed
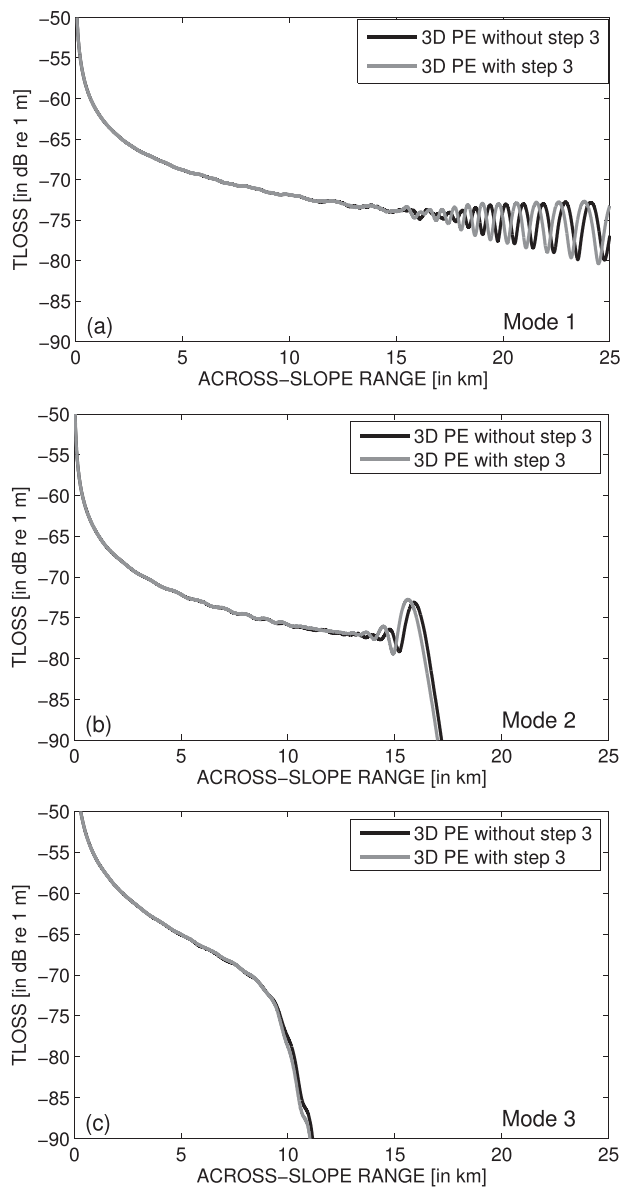
FIG. 4. Transmission loss (in dB re 1 m) curves at a receiver depth of 30 m in the across-slope direction $\theta = 90°$ corresponding to 3D PE solutions obtained initializing by (a) mode 1, (b) mode 2, and (c) mode 3, and computing without step 3 (black curves) and with step 3 (gray curves). For each modal initialization, both 3D PE solutions were computed using $n_p = 2 = m_p$.

in Figs. 5(b) and 5(c). Though it is clear from the previous TL-versus-range curve comparisons that differences exist between these two 3D PE solutions [see also the error plots shown in Figs. 5(d) and 6(d)], these differences do not modify significantly the interference structures of the field and are even hardly visible when comparing the two 3D PE fields at a fixed depth, see Figs. 6(b) and 6(c). This shows that the 3D PE solution obtained without step 3, though less accurate than the 3D PE solution obtained with step 3, is still able to reproduced the main 3D effects.

V. CONCLUSION

In this paper, a new 3D PE model, that includes a leading-order cross-term correction in its formulation, has
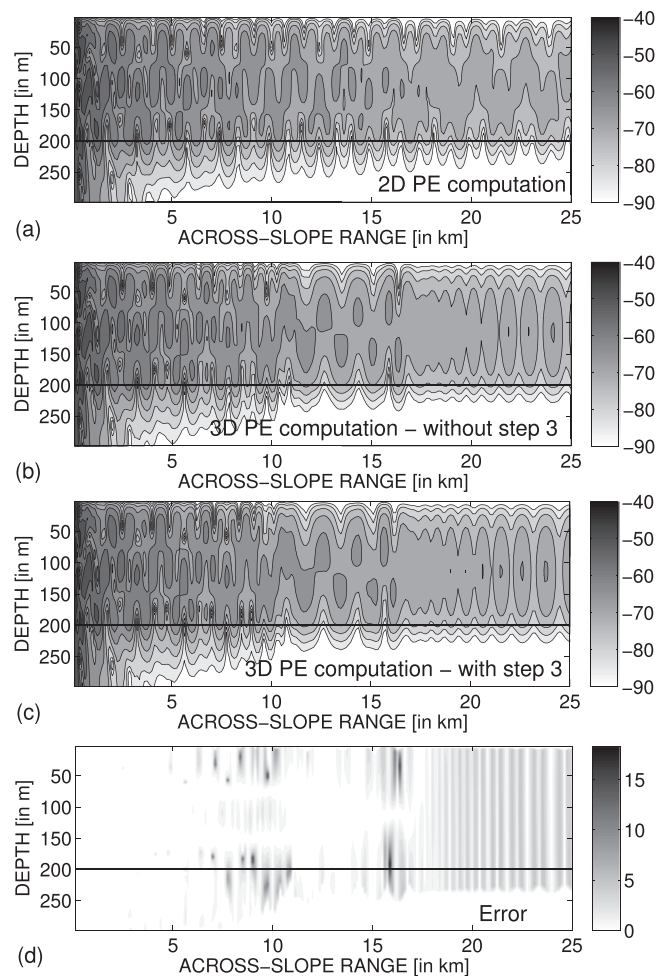

FIG. 5. Transmission loss (vertical slices at constant azimuth, across-slope) corresponding to a 2D PE computation [subplot (a)] and 3D PE computations without [subplot (b)] and with [subplot (c)] step 3. The 3D solutions correspond to a Padé 2 expansion in both depth and azimuth ($n_p = 2 = m_p$). On each subplot, the sediment interface (at a constant depth of 200 m) is indicated by a solid line. Subplot (d) shows the error (obtained subtracting values in dB of transmission-loss fields) between the two 3D PE solutions displayed in subplots (b) and (c).

been derived and benchmarked against a 3D reference solution based on an image source method. Of particular interest, the discretized leading-order cross-term operator has been incorporated in an existing numerical scheme by simply adding a third step in the original 2-step based splitting method. It has been shown that the quality of the comparisons with the 3D reference solution deteriorates when 3D PE solutions are computed ignoring step 3 (i.e., retaining only steps 1 and 2 in the calculations) and a very good agreement between the 3D reference solution and the fully wide-angle 3D PE solution that handles the leading-order cross term has been observed, which confirms that the now-fully wide-angle 3D PE model can handle larger propagation angles. Note that the cross-multiplied terms, including the leading-order cross term considered here, are neglected in most of the existing 3D PE models. The numerical technique proposed in this paper could be used in the future to update in a straightforward manner any 3D PE algorithms[1–3,5,6,9] that use a splitting numerical technique similar to the ADI method.
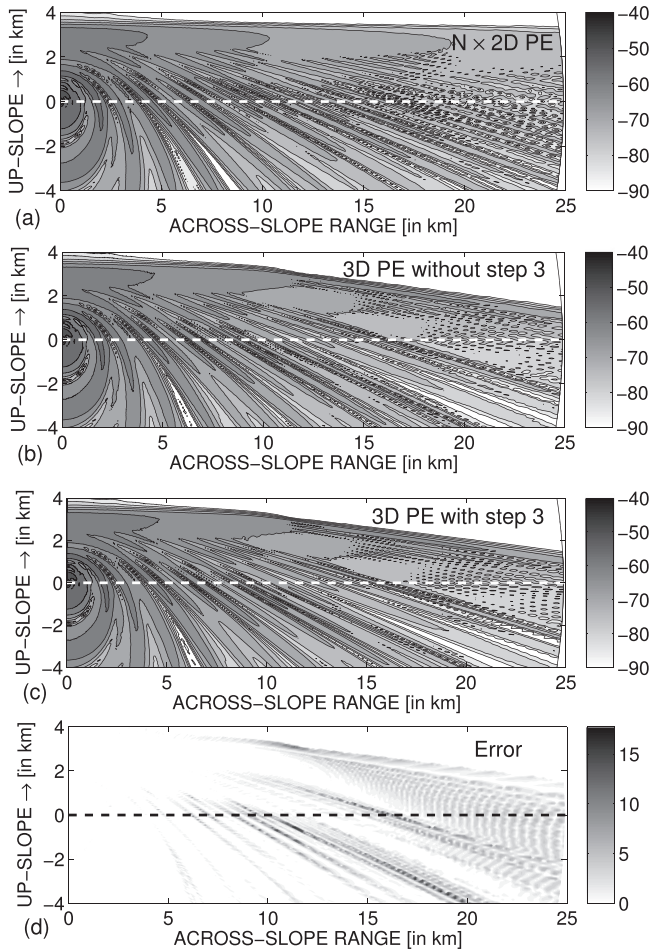
Frédéric Sturm

FIG. 6. Transmission loss (horizontal slices at a receiver depth of 30 m) corresponding to a 2D PE computation [subplot (a)] and 3D PE computations without [subplot (b)] and with [subplot (c)] step 3. Both 2D and 3D PE solutions correspond to a Padé 2 expansion in both depth and azimuth ($n_p = 2 = m_p$). On each subplot, the across-slope direction (i.e., $\theta = 90°$) is indicated by a dashed line. Subplot (d) shows the error (obtained subtracting values in dB of transmission-loss fields) between the two 3D PE solutions displayed in subplots (b) and (c).

As explained in Sec. III, handling the leading-order cross term considerably slows down the computations. The workload of the algorithm to solve for step 3 is relatively heavy (in comparison to other approaches that preserve the advantages of ADI methods[10,12]) in terms of both memory storage and central processing unit (CPU) time considerations. The numerical algorithm proposed in this paper is comparable to other 3D PE formulations[16,18,19,23] that lead to large sparse 9-diagonal matrices with block-tridiagonal structures and thus require great computational resources and specific iterative methods to inverse the resulting linear systems at each step of the marching algorithm. Our objective in this paper was to analyze the importance of incorporating such a cross term, without focusing on CPU time considerations nor memory storage limitations (though convinced of their importance). Obviously, acceleration of the iterative algorithm should be improved by testing other inversion algorithms and by using other preconditioners. In addition, following the approach used in step 2 to discretize the second-order azimuthal operator, a higher-order centered

FD scheme should be used in step 3 to discretize the cross term. This is currently underway.

Let us conclude this section with one last remark. For the 3D wedge-shaped synthetic test case considered here, it has been shown that higher-order 3D PE computations carried out ignoring step 3, though less accurate, allow a reasonably good description of all the 3D effects present in the waveguide. The comparisons presented in this paper (see also in Ref. 10) show that incorporating cross-derivative terms is something that is really needed for meticulous and rigorous benchmark comparisons. However, in practical situations and/or when dealing with real problems that have wedge-shaped geometries with moderate bottom slopes, 3D PE computations carried out ignoring step 3 still offer a sufficient description of most 3D effects and could be used as a first approach. The user is then free to decide whether he needs or can afford more accurate but longer 3D PE computations handling cross-derivative terms or not.

[1]M. Collins and S. Ching-Bing, "A three-dimensional parabolic equation model that includes the effects of rough boundaries," J. Acoust. Soc. Am. **87**, 1104–1109 (1990).

[2]D. Lee, G. Botseas, and W. Siegmann, "Examination of three-dimensional effects using a propagation model with azimuth-coupling capability (FOR3D)," J. Acoust. Soc. Am. **91**, 3192–3202 (1992).

[3]J. Fawcett, "Modeling three-dimensional propagation in an oceanic wedge using parabolic equation methods," J. Acoust. Soc. Am. **93**, 2627–2632 (1993).

[4]K. Smith, "A three-dimensional propagation algorithm using finite azimuthal aperture," J. Acoust. Soc. Am. **106**, 3231–3239 (1999).

[5]J. Arvelo and A. Rosenberg, "Three-dimensional effects on sound propagation and matched-field processor," J. Comput. Acoust. **9**, 17–39 (2001).

[6]G. Brooke, D. Thomson, and G. Ebbeson, "PECan: A Canadian parabolic equation model for underwater sound propagation," J. Comput. Acoust. **9**, 69–100 (2001).

[7]C. F. Chen, Y.-T. Lin, and D. Lee, "A three-dimensional azimuthal wide-angle model," J. Comput. Acoust. **7**, 269–288 (1999).

[8]F. Sturm, "Numerical study of broadband sound pulse propagation in three-dimensional oceanic waveguides," J. Acoust. Soc. Am. **117**, 1058–1079 (2005).

[9]M. E. Austin and N. R. Chapman, "The use of tessellation in three-dimensional parabolic equation modeling," J. Comput. Acoust. **19**, 221–239 (2011).

[10]Y.-T. Lin, J. Collis, and T. Duda, "A three-dimensional parabolic equation model of sound propagation using higher-order operator splitting and Padé approximants," J. Acoust. Soc. Am. **132**, EL364–EL370 (2012).

[11]Y.-T. Lin, T. Duda, and A. Newhall, "Three-dimensional sound propagation models using the parabolic-equation approximation and the split-step Fourier method," J. Comp. Acoust. **21**, 250018 (2013).

[12]Y.-T. Lin and T. Duda, "A higher-order split-step Fourier parabolic-equation sound propagation solution scheme," J. Acoust. Soc. Am. **132**, EL61–EL67 (2012).

[13]K. Heaney, R. L. Campbell, M. Zampolli, and M. Prior, "Observation and modelling of three-dimensional basin scale acoustics," in *Proceedings of the 1st International Conference and Exhibition on Underwater Acoustics*, edited by J. S. Papadakis and L. Björno (2013), 1686 pp.

[14]F. Jensen, W. Kuperman, M. Porter, and H. Schmidt, *Computational Ocean Acoustics* (Springer, New York, 2011).

[15]F. Tappert, "The parabolic approximation method," in *Wave Propagation and Underwater Acoustics, Lecture Notes in Physics*, Vol. 70 (Springer, New York, 1977), pp. 224–287.

[16]W. Siegmann, G. Kriegsmann, and D. Lee, "A wide-angle three-dimensional parabolic wave equation," J. Acoust. Soc. Am. **78**, 659–664 (1985).

[17]D. Lee and W. Siegmann, "A mathematical model for the 3-dimensional ocean sound propagation," Math. Model. **7**, 143–162 (1986).

[18]F. Sturm and N. Kampanis, "Accurate treatment of a general sloping interface in a finite-element 3-D narrow-angle PE model," J. Comput. Acoust. **15**, 285–318 (2007).

[19]J. M. Collis, "Three-dimensional underwater sound propagation using a split-step Padé parabolic equation solution (A)," J. Acoust. Soc. Am. **130**, 2528 (2011).

[20]R. Baer, "Propagation through a three-dimensional eddy including effects on an array," J. Acoust. Soc. Am. **69**, 70–75 (1981).

[21]D. Yevick and D. Thomson, "Split-step/finite-difference and split-step/Lanczos algorithms for solving alternative higher-order parabolic equations," J. Acoust. Soc. Am. **96**, 396–405 (1994).

[22]D. Yevick and D. Thomson, "A hybrid split-step/finite-difference PE algorithm for variable-density media," J. Acoust. Soc. Am. **101**, 1328–1335 (1997).

[23]D. Lee and M. Schultz, *Numerical Ocean Acoustics Propagation in Three Dimensions* (World Scientific, Singapore, 1995).

[24]A. Bamberger, B. Engquist, L. Halpern, and P. Joly, "Higher order paraxial wave equation approximations in heterogeneous media," SIAM J. Appl. Math. **48**, 129–154 (1988).

[25]M. Collins, "Higher order Padé approximations for accurate and stable elastic parabolic equations with application to interface wave propagation," J. Acoust. Soc. Am. **89**, 1050–1057 (1991).

[26]F. Sturm and J. Fawcett, "On the use of higher-order azimuthal schemes in 3-D PE modeling," J. Acoust. Soc. Am. **113**, 3134–3145 (2003).

[27]A. Bayliss, C. I. Goldstein, and E. Turkel, "An iterative method for the Helmholtz equation," J. Comp. Phys. **49**, 443–457 (1983).

[28]R. Greene, "The rational approximation to the acoustic wave equation with bottom interaction," J. Acoust. Soc. Am. **76**, 1764–1773 (1984).

[29]E. Westwood, "Broadband modeling of the three-dimensional penetrable wedge," J. Acoust. Soc. Am. **92**, 2212–2222 (1992).

[30]E. Westwood, "Complex ray solutions to the 3-D wedge ASA benchmark problems," J. Acoust. Soc. Am. **109**, 2333 (2001).